

Midnight density and temperature maxima, and thermospheric dynamics in Whole Atmosphere Model simulations

R. A. Akmaev,¹ F. Wu,² T. J. Fuller-Rowell,² H. Wang,² and M. D. Iredell³

Received 10 May 2010; accepted 6 July 2010; published 28 August 2010.

[1] Hydrostatic expansion in a gravity field of an atmospheric layer with elevated temperatures, such as the long known thermospheric midnight temperature maximum (MTM), results in a total mass density increase at a given altitude above the layer. Long-term simulations with the Whole Atmosphere Model reveal a noticeable midnight density maximum (MDM), appropriately lagging behind the MTM at the same height. The MDM magnitude, timing, and variability are in good agreement with available in-situ observations. Of particular importance is the observation of a downward phase progression of the MDM peak time obtained from the San Marco satellites and closely reproduced in the model results. This is consistent with the suggestion, made over 30 years ago, that both the MTM and MDM are driven by tidal waves, in particular, the terdiurnal tide propagating upward from the lower atmosphere and interacting with a diurnally varying ion drag. The accompanying wind variations are also found in good agreement with radar observations, which first related them to the nighttime ionosphere collapse in the early 1970s.

Citation: Akmaev, R. A., F. Wu, T. J. Fuller-Rowell, H. Wang, and M. D. Iredell (2010), Midnight density and temperature maxima, and thermospheric dynamics in Whole Atmosphere Model simulations, *J. Geophys. Res.*, *115*, A08326, doi:10.1029/2010JA015651.

1. Introduction

[2] Mass-spectrometer observations from the Orbital Geophysical Observatory 6 (OGO-6) in the early 1970s revealed low-latitude secondary maxima of N₂ and O densities near local midnight in addition to the main maximum in the afternoon. Under the assumption of diffusive equilibrium the enhanced densities were related to the thermospheric midnight temperature maximum (MTM) [Mayr *et al.*, 1979], first discovered in radar observations of ion temperatures [Harper, 1973] and soon after confirmed by in-situ measurements of neutral temperatures from the Atmosphere Explorer E (AE-E) [Spencer *et al.*, 1979]. Mayr *et al.* [1979] suggested that the terdiurnal and higher-order tidal harmonics might play an important role in generating the MTM via nonlinear interactions with a diurnally varying ion drag.

[3] While the MTM has since been observed remotely, e.g., by passive optical instruments from the ground [Meriwether *et al.*, 2008], densities of thermospheric species or the total mass density are typically measured in situ by mass spectrometers or estimated from satellite drag data such as the recent observations by the Challenging Mini-satellite Payload (CHAMP) [Liu *et al.*, 2005]. A systematic study of the midnight density maximum (MDM) was presented by

Arduini *et al.* [1997] using drag balance instrument data from a pair of San Marco (SM) satellites flown in low-inclination orbits in 1971 and 1988. Good local time resolution and height coverage allowed to compile a climatology of the MDM magnitude and peak time depending on season, altitude, and solar activity. In particular, a downward phase progression of the MDM was observed, consistent with the upward propagation of tides [Arduini *et al.*, 1997].

[4] Akmaev *et al.* [2009] presented first realistic simulations of the MTM by the Whole Atmosphere Model (WAM) clearly demonstrating its close connection to tides, in particular, the terdiurnal tide propagating up from the lower thermosphere [e.g., Akmaev, 2001]. The purpose of this note is to present WAM simulations of the MDM and its variability and analyze possible connections to the MTM and variations of other thermospheric parameters.

2. Model

[5] WAM is an extension of the operational weather prediction Global Forecast System (GFS) general circulation model (GCM) to the top of the atmosphere [Akmaev *et al.*, 2008; Akmaev and Juang, 2008]. The model is being built to study and potentially develop a capability to predict the effects of lower atmosphere dynamics and variability on the upper atmosphere and ionosphere [Fuller-Rowell *et al.*, 2008, 2010].

[6] As most weather and climate GCMs, WAM is a hydrostatic model with a terrain-following hybrid vertical coordinate converting to pure pressure in the stratosphere. According to the ideal gas law, density decreases with

¹NOAA Space Weather Prediction Center, Boulder, Colorado, USA.

²CIRES, University of Colorado, Boulder, Colorado, USA.

³NOAA Environmental Modeling Center, Camp Springs, Maryland, USA.

Report Documentation Page

Form Approved
OMB No. 0704-0188

Public reporting burden for the collection of information is estimated to average 1 hour per response, including the time for reviewing instructions, searching existing data sources, gathering and maintaining the data needed, and completing and reviewing the collection of information. Send comments regarding this burden estimate or any other aspect of this collection of information, including suggestions for reducing this burden, to Washington Headquarters Services, Directorate for Information Operations and Reports, 1215 Jefferson Davis Highway, Suite 1204, Arlington VA 22202-4302. Respondents should be aware that notwithstanding any other provision of law, no person shall be subject to a penalty for failing to comply with a collection of information if it does not display a currently valid OMB control number.

1. REPORT DATE 28 AUG 2010	2. REPORT TYPE	3. DATES COVERED 00-00-2010 to 00-00-2010			
4. TITLE AND SUBTITLE Midnight density and temperature maxima, and thermospheric dynamics in Whole Atmosphere Model simulations		5a. CONTRACT NUMBER			
		5b. GRANT NUMBER			
		5c. PROGRAM ELEMENT NUMBER			
6. AUTHOR(S)		5d. PROJECT NUMBER			
		5e. TASK NUMBER			
		5f. WORK UNIT NUMBER			
7. PERFORMING ORGANIZATION NAME(S) AND ADDRESS(ES) University of Colorado, Boulder, CIRES, Boulder, CO, 80309		8. PERFORMING ORGANIZATION REPORT NUMBER			
9. SPONSORING/MONITORING AGENCY NAME(S) AND ADDRESS(ES)		10. SPONSOR/MONITOR'S ACRONYM(S)			
		11. SPONSOR/MONITOR'S REPORT NUMBER(S)			
12. DISTRIBUTION/AVAILABILITY STATEMENT Approved for public release; distribution unlimited					
13. SUPPLEMENTARY NOTES					
14. ABSTRACT					
15. SUBJECT TERMS					
16. SECURITY CLASSIFICATION OF:			17. LIMITATION OF ABSTRACT Same as Report (SAR)	18. NUMBER OF PAGES 8	19a. NAME OF RESPONSIBLE PERSON
a. REPORT unclassified	b. ABSTRACT unclassified	c. THIS PAGE unclassified			

increasing temperature at fixed pressure. At the same time constant pressure surfaces rise to higher altitudes. As a result, density at a given altitude should increase above a layer of heating. A density enhancement is therefore expected to develop above a layer of elevated temperatures such as the MTM.

[7] The height z of a given pressure level depends on the acceleration of gravity $g(z)$. In lower atmospheric GCMs the assumption of a shallow atmosphere and constant g is traditionally employed [Phillips, 1966]. The GFS top pressure level of about 0.3 hPa approximately corresponds to an altitude of 57 km. The model thus extends to just about 1% of Earth's radius r_E above the surface and the assumption of constant g is a very good approximation. (It is of some interest to note here parenthetically that this "shallow" model domain contains almost 99.97% of the mass of the atmosphere.) In "deep" GCMs spanning hundreds of kilometers vertically the assumption of constant gravity is no longer satisfactory. The continuous use of constant, albeit reduced, g in some upper-atmospheric models is sometimes misinterpreted as that the implementation of height-dependent gravity acceleration in hydrostatic GCMs may be nontrivial [e.g., Deng et al., 2008].

[8] It should be noted first that the large-scale resolved dynamics equations of hydrostatic models in pressure (or pressure-related) coordinates use geopotential Φ and not the height of pressure levels to calculate the horizontal pressure gradient forces. The gravity acceleration does not explicitly enter these equations and in this regard the model output may be considered independent of whether or not it is constant and postprocessed with appropriately chosen $g(z)$. However, some empirical models used in GCMs, parameterizations of certain subgrid processes such as vertical diffusion, or coupling with models of other physical domains such as the plasmasphere often require heights of pressure levels during runtime. For these purposes height calculations may be readily implemented in hydrostatic GCMs under quite general assumptions about $g(z)$.

[9] At every model grid point on the globe an increment of geopotential $\Delta\Phi$ between the surface pressure p_s (generally varying with location and time) and a given pressure level p is routinely calculated by integrating the static equation

$$\Delta\Phi = \int_{\Phi_s}^{\Phi} d\Phi = \int_p^{p_s} \frac{RT}{p} dp, \quad (1)$$

where R is the specific gas constant (the universal gas constant divided by the mean molar mass), T temperature, and Φ_s the surface geopotential. Obviously, the integrand on the right-hand side increases with increasing T or R (decreasing molar mass). Note also that $g(z)$ is "hidden" inside the geopotential differential in (1)

$$d\Phi = g(z)dz, \quad (2)$$

and so never enters the large-scale dynamical equations explicitly. Assuming Newtonian gravity

$$g(z) = g_0 \frac{r_E^2}{(r_E + z)^2}, \quad (3)$$

where $g_0 = g(0)$ is gravity at the sea level ($z = 0$), which may even be allowed to depend on geographic coordinates if

desired. Substituting (3) and (2) into (1), integrating, and solving for z a conversion from geopotential to height follows:

$$z = \frac{r_E \Phi}{g_0 r_E - \Phi}, \quad (4)$$

where $\Phi = \Delta\Phi + \Phi_s$, and the surface geopotential is found by substituting the surface elevation z_s into (4)

$$\Phi_s = g_0 r_E \frac{z_s}{r_E + z_s}.$$

A more common expression $\Phi_s \approx g_0 z_s$ is also a good approximation because $|z_s| \ll r_E$. The gravity acceleration may then be calculated using (3).

3. Results and Discussion

[10] WAM has been run for over a year under fixed low solar and quiet geomagnetic activity conditions. Figures 1 (left) and 2 (left) present relative density variations at 400 km and latitudes $\pm 20^\circ$, close to locations where most available observations have been obtained, in March and December, respectively. For each latitude two different UT/longitude sectors are also shown. Density peaks occur between about 0 and 2 LT, depending on location and season, with magnitudes ranging from about 10% to over 20% consistent with direct SM observations [Arduini et al., 1997]. Strong day-to-day variability is evident as are variations from one longitude sector to the other.

[11] The MDM peak normally lags behind the MTM at the same altitude because it is an integral effect of enhanced temperatures over some underlying layer and both the MDM and MTM peaks occur earlier at higher altitudes (see also Figure 3), consistent with the upward tide propagation [Arduini et al., 1997; Akmaev et al., 2009]. For comparison Figures 1 (middle) and 2 (middle) present relative temperature variations at a substantially lower altitude of 300 km, which are roughly in phase with the density variations at 400 km.

[12] Figure 3 presents the vertical structure of the MDM and the underlying MTM at 30°N on two days one week apart in December. The downward phase progression is in excellent agreement with the SM observations [Arduini et al., 1997] and clearly indicates that both the MTM and MDM propagate upward from the lower thermosphere. The MTM typically leads the MDM at the same altitude by about one hour, because the latter is an integral effect of the former over some layer below. Conversely, at any given instance the MTM and MDM are always separated in space either vertically with the MDM occurring above the MTM at the same longitude or lagging eastward of the MTM at the same height. It actually follows from the equation of state that the peaks in temperature and density cannot occur in the same place at the same time (see also Appendix A for a more quantitative discussion of phase lags between temperature, density, pressure, and other variables).

[13] The day-to-day variability of the phenomena is clearly seen from a comparison of the two days in Figure 3. The stronger MDM at higher altitudes on December 4 is driven by a stronger MTM above 200 km. Conversely, there is a stronger MDM developing at 200–250 km on December 11

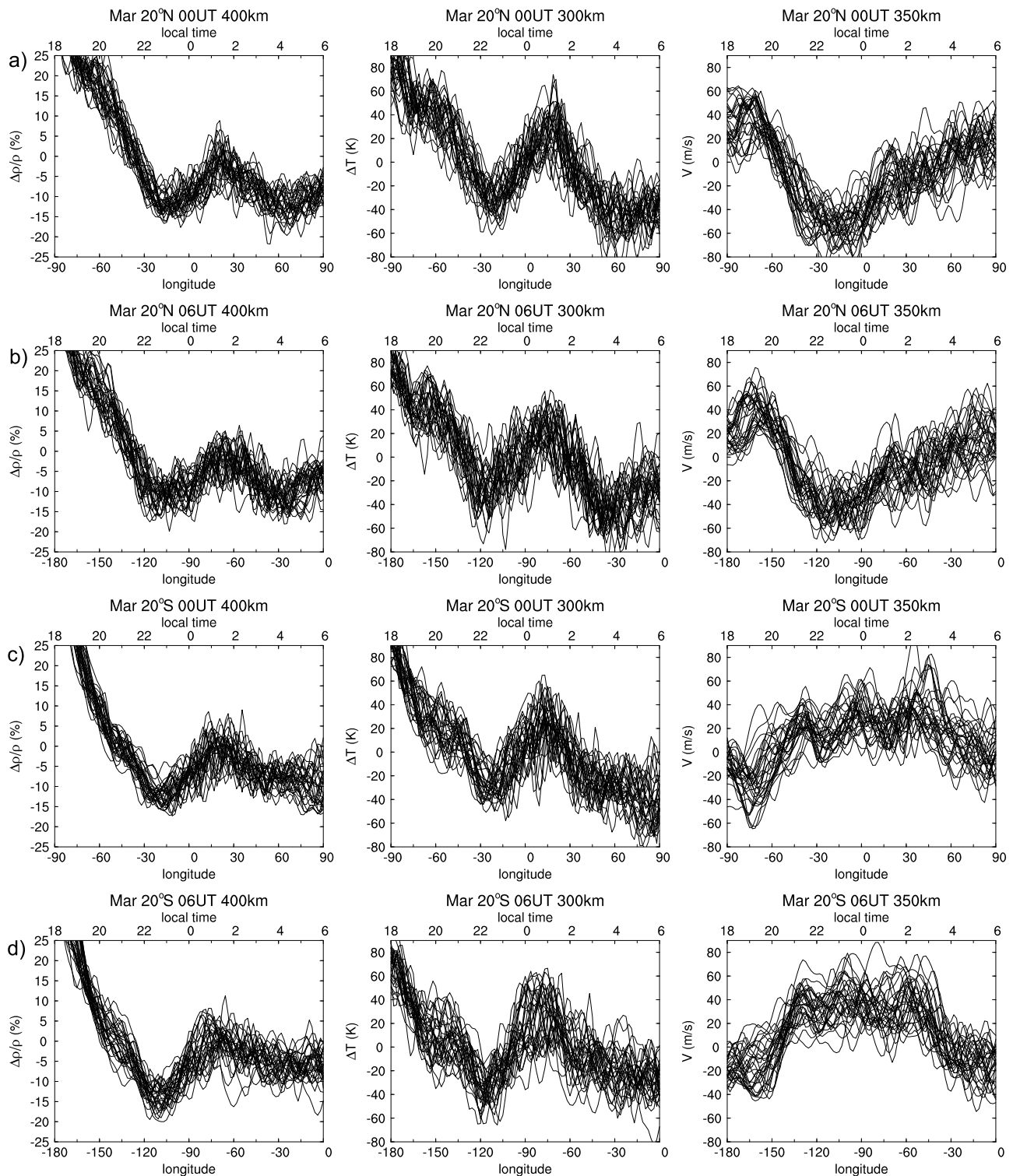


Figure 1. Snapshots of WAM simulations for March with each line representing 1 day: (left) Relative density deviation from the zonal mean (%) at 400 km, (a and b) 20°N and (c and d) 20°S, at 00 UT (Figures 1a and 1c) and 06 UT (Figures 1b and 1d). (middle) Same but for temperature deviation from the zonal mean (K) at 300 km. (right) Same but for meridional wind (ms^{-1} , positive Northward) at 350 km.

in response to a stronger MTM at even lower altitudes. The temperature and density maxima occurring at lower altitudes near midnight are clearly related to another upward propagating tidal branch preceding the main features by about

6 hours. Interestingly, the SM-5 observations obtained during higher solar activity show the MDM sometimes occurring earlier at 250–300 km than above [Arduini *et al.*, 1997]. A possible explanation is that the satellite might have observed

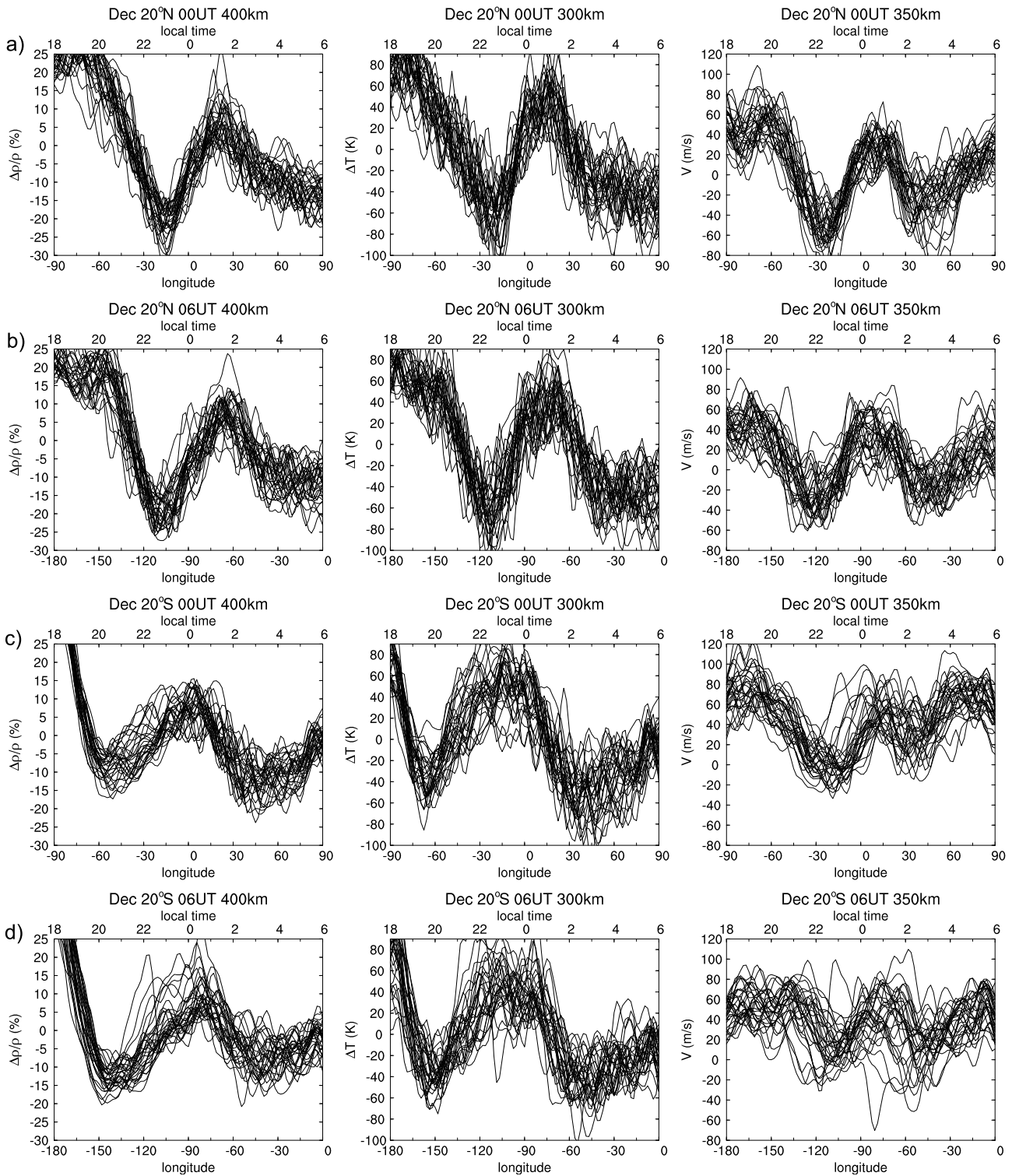


Figure 2. Same as Figure 1 but for December.

the second tidal branch at these lower altitudes. Note also that at higher solar activity this low-altitude MDM would be displaced higher up compared to the low-activity case presented in Figure 3. At higher altitudes the second tidal branch manifests as secondary peaks in both temperature

and density between about 18 and 20 LT in agreement with temperature observations from the ground (J. W. Meriwether, personal communication, 2009). These secondary density peaks also appear to be related to what *Forbes et al.* [2008] identified as an evening terminator wave in CHAMP observa-

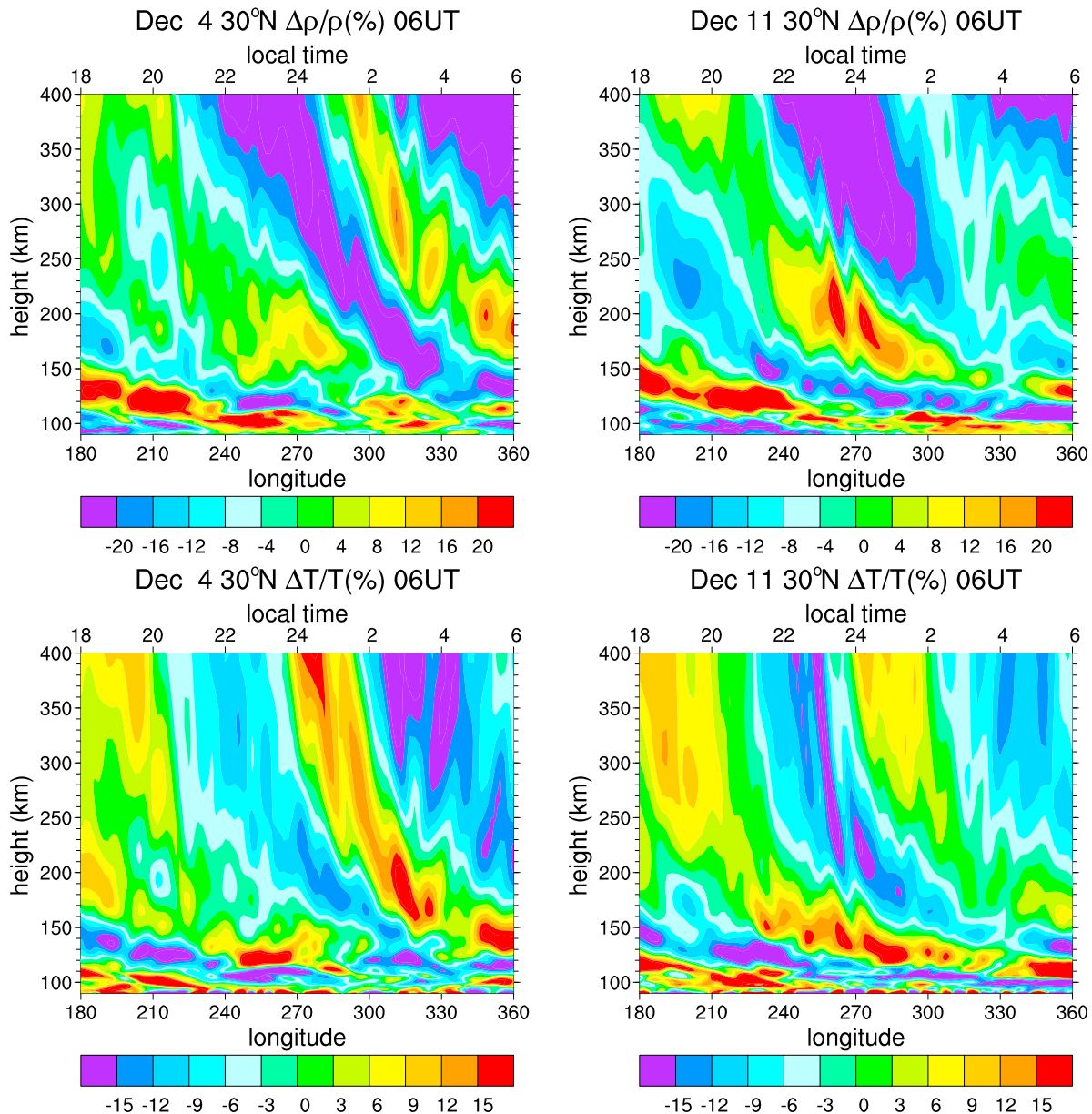


Figure 3. (top) Snapshots of relative density deviation from the zonal mean (%) at 06 UT on (left) December 4 and (right) December 11 as a function of height and longitude/local time. (bottom) Same but for relative temperature deviation from the zonal mean (%).

tions near 400 km. Note however that these features can be traced down to morning hours in the lower thermosphere.

[14] Radar observations at 350 km in the ionospheric F region over Arecibo revealed peak equatorward meridional winds between about 22 and 00 LT decreasing or reversing poleward shortly after midnight in winter and spring [Behnke and Harper, 1973; Harper, 1973]. The wind reversal was associated with a regularly observed nighttime ionosphere collapse because of plasma being driven downward along the magnetic field lines. Harper [1973] additionally observed a peak in ion temperatures at about the same time. The meridional wind reversal at 350 km is also reproduced in WAM simulations at 20°N in excellent

agreement with these observations (Figures 1a (right), 1b (right), 2a (right), and 2b (right)). Note that in December (Figure 2) the winds turn equatorward again for a short time before dawn, whereas at equinox (Figure 1) the poleward reversal continues through to dawn without another reversal. These features are all generally consistent with the observations [Behnke and Harper, 1973; Harper, 1973].

[15] Optical observations in Southern tropics in equinox and winter [Meriwether et al., 2008] also associate the MTM with a preceding peak of the equatorward meridional wind abating or turning poleward some time after the MTM peak. This is generally consistent with the WAM simulations presented here, especially in March (Figure 1). Note also

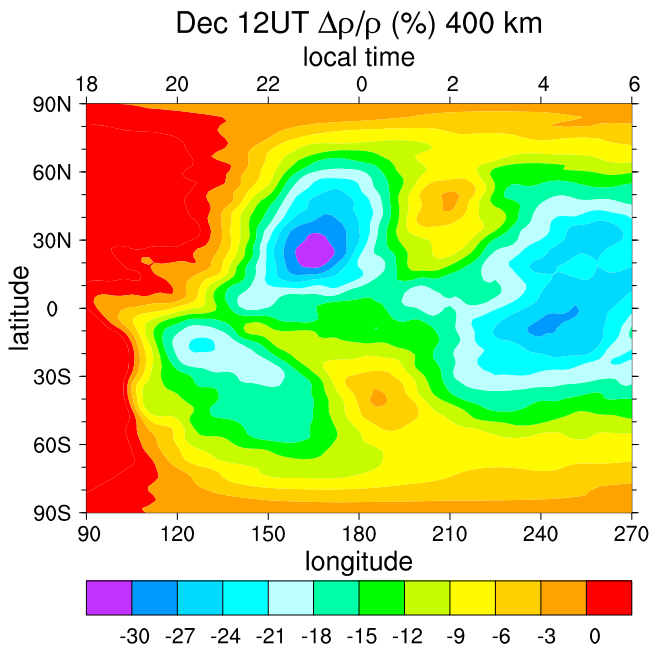


Figure 4. December monthly mean relative density deviation from the zonal mean (%) at 400 km and 12 UT as a function of latitude and longitude/local time.

that the airglow observed by *Meriwether et al.* [2008] comes from lower altitudes generally corresponding to later local times of maxima (Figure 3).

[16] The observed relation between the direction of meridional winds and the MTM is to be expected from theory of strongly damped tidal waves [Volland and Mayr, 1972]. Strong tidal dissipation is evidenced by the cessation of the exponential growth of wave amplitudes with altitude above about 150–200 km [Akmaev et al., 2009]. In this regime the pressure gradient force is almost entirely balanced by frictional forces due to ion drag and molecular viscosity in the horizontal momentum balance equation. As a result, tidal oscillations of the poleward meridional wind are approximately in phase with oscillations of pressure at the same height (or, equivalently, of geopotential at the same pressure) and the eastward zonal wind lags by a quarter period [Volland and Mayr, 1972].

[17] It should be noted again that because of hydrostatic balance pressure oscillations at a given height are an integral effect of temperature variations in the underlying layers. Therefore the surge of equatorward winds observed at a given height, say 350 km, corresponds to a pressure trough resulting from a temperature minimum preceding the MTM at lower levels (Figure 3). The meridional wind reversal toward the poles occurs approximately during the MTM at the same level and the poleward winds maximize some time after that, driven by a pressure bulge when temperatures below rise. This interpretation is at variance with the two-dimensional conceptual model of *Meriwether et al.* [2008] suggesting that both the pressure bulge and the MTM are created simultaneously by horizontal tidal winds converging at low latitudes near midnight. A pressure bulge at a given height cannot be created or supported unless

temperatures below rise as well (Figure 3). (See also Appendix A.)

[18] An example of the MDM horizontal structure at solstice is presented in Figure 4. It is similar to the V-shaped form of the MTM with peaks occurring earlier at lower latitudes and earlier in summer than in winter at the same latitude as observed from AE-E [Herrero and Spencer, 1982] and simulated by WAM [Akmaev et al., 2009]. The feature clearly extends to midlatitudes, consistent with ground-based observations of the airglow brightness wave commonly associated with the MTM [Colerico et al., 2006; Martinis et al., 2006].

4. Conclusion

[19] First WAM simulations of the MDM are in reasonably good agreement with available in-situ observations [Arduini et al., 1997], including the crucial observation of its downward phase progression. While the SM observations suggest somewhat larger amplitudes in equinox, our simulations show larger magnitudes and stronger variability in solstice, especially in the winter hemisphere, consistent with the more chaotic dynamics in the lower atmosphere. Note that the day-to-day variability presented here comes entirely from below as the solar and geomagnetic forcings have been kept constant at low levels in these simulations. The variability may only be expected to increase with additional variable and sporadic forcings from above.

[20] Even the limited seasonal and daily variability of the MDM magnitude and timing seen in WAM simulations may have important implications for interpretation of in-situ satellite observations. Spacecraft in high-inclination orbits (e.g., OGO-6 and CHAMP) inevitably average out and underestimate the MDM magnitude as they slowly precess through local time and sample different longitude sectors. On the other hand, satellites in low-inclination orbits (e.g., AE-E and San Marco) usually offer a better local time resolution and sampling but are limited in their latitude coverage. The full global extent, magnitude, and variability of the MTM/MDM phenomena may only be ascertained by combining data from in-situ instruments in complementary orbits with remote sensing, including by radars and optical instruments on the ground.

[21] It remains to be seen whether such a localized but recurring feature as the MDM could substantially affect satellite orbits but it is encouraging that numerical models such as WAM are now capable of reproducing it in reasonable agreement with observations. Our results show that the MDM, MTM, and accompanying thermospheric wind variations are just different manifestations of a forcing imposed by tidal waves propagating up from the lower atmosphere and interacting with dissipative processes in the upper atmosphere and ionosphere.

Appendix A: Polarization Relations in Hydrostatic Dissipative Waves

[22] The purpose of this appendix is to obtain quantitative estimates and gain further insights into relations between different variables, in particular the relative amplitudes and phases of temperature, pressure, and density oscillations. However, instead of employing a full dynamical theory

[e.g., *Volland and Mayr*, 1972, 1973] simple diagnostics of the simulation results presented here are developed subject to constraints imposed by the hydrostatic balance and the equation of state under reasonable simplifying assumptions. An idealized case of a temperature wave propagating upward and westward (Figure 3) is considered. Note that the westward tilt of the features in Figure 3 implies that, as they move westward, the phase, commonly defined as the local time of maximum, propagates downward, a familiar feature for upward propagating waves.

[23] An isothermal background is assumed and variations of the mean molecular mass and gravity are neglected. Under these conditions the background scale height \bar{H} is constant, where the overbar denotes mean quantities. A harmonic vertical structure is adopted

$$\frac{T'}{\bar{T}} = \Theta \cos kz, \quad (\text{A1})$$

where the relative wave amplitude Θ is also assumed saturated at a constant value because of strong dissipation [*Akmaev et al.*, 2009; *Volland and Mayr*, 1972]. The prime denotes wave induced deviations from the mean and k is the vertical wave number. Substituting (A1) into the static equation

$$\frac{dp}{p} = -\frac{dz}{\bar{H}},$$

integrating vertically, and linearizing under the assumption of small temperature amplitudes (see Figure 3), the following expression for relative pressure variations results:

$$\frac{p'}{\bar{p}} \approx P \sin kz = P \cos\left(kz - \frac{\pi}{2}\right), \quad (\text{A2})$$

where the pressure amplitude

$$P = \frac{\Theta}{(kH)}. \quad (\text{A3})$$

Relation (A2) states that at any instance the pressure oscillation lags behind the temperature oscillation by a quarter wavelength in height, i.e., the pressure maximum occurs above the temperature maximum. Equivalently, the pressure maximum lags the MTM by a quarter period at the same altitude. This means that at a given height the pressure maximum occurs after the MTM approximately near the node between the temperature maximum and the following temperature minimum, as was qualitatively suggested in Section 3. Tidal theory also predicts that the poleward meridional wind maximum corresponds to the pressure maximum [*Volland and Mayr*, 1972].

[24] Substituting (A1) and (A2) into the linearized equation of state

$$\frac{\rho'}{\bar{\rho}} \approx \frac{p'}{\bar{p}} - \frac{T'}{\bar{T}},$$

the following expression for relative density variations is obtained:

$$\frac{\rho'}{\bar{\rho}} \approx D \cos\left(kz - \frac{\pi}{2} - \alpha\right), \quad (\text{A4})$$

where the density amplitude

$$D = \sqrt{P^2 + \Theta^2}. \quad (\text{A5})$$

There is an additional phase lag for the density oscillation

$$\alpha = \arctan \frac{\Theta}{P} \geq 0. \quad (\text{A6})$$

According to (A1) and (A2) the pressure maximum occurs roughly at the node of temperature fluctuations. Because at given pressure density is inversely proportional to temperature, the density fluctuation maximizes somewhere between the pressure maximum and the following temperature minimum resulting in an additional phase delay α depending on the relative amplitudes of pressure and temperature (A6).

[25] The diagnostic relations obtained here are only based on the assumptions regarding the vertical structure and the direction of propagation of the temperature perturbation. No information on the horizontal structure is needed, of course with the exception of wind variations, driven by the horizontal pressure gradients. For these the predictions of full dynamical theory have to be invoked [*Volland and Mayr*, 1972]. As follows from (A3), the results also depend on the vertical scales involved as detailed below.

[26] In WAM simulations (Figure 3), the vertical scale of the temperature wave is roughly comparable to the scale height ($kH \sim 1$). The relative pressure and density amplitudes P and D are then of the same order as the temperature amplitude Θ and remain constant according to (A3) and (A5). The density maximum lags the pressure maximum by $\alpha \approx \pi/4$ or by an additional one-eighth of wavelength or period (A6).

[27] Although not directly related to the MTM and MDM, two other limiting cases may be considered for completeness. At very long vertical scales ($kH \ll 1$) this analysis is not entirely applicable because there is essentially no sinusoidal structure in the vertical. However some useful estimates may still be obtained. Because the temperature variations are practically in phase at all altitudes, the pressure oscillations should then be roughly in phase with temperature, perhaps just slightly lagging behind unlike in (A2). Because contributions of temperature variations at all levels add up constructively, the pressure perturbation is expected to grow in amplitude with height. Above some altitude the relative pressure amplitude will inevitably become greater than the temperature amplitude ($P \gg \Theta$) in agreement with (A3), driving up the density and wind amplitudes as well [*Volland and Mayr*, 1973]. It follows from (A5) and (A6) that under these conditions the density and pressure oscillations have comparable relative amplitudes ($D \approx P$) and are in phase ($\alpha \rightarrow 0$).

[28] The case of very small vertical scales ($kH \gg 1$) describes shallow low-frequency gravity waves for which, according to (A3), the relative pressure amplitude becomes small compared to the temperature amplitude ($P \ll \Theta$) [*Hines*, 1960]. It then follows from (A4) or (A6) that the relative density and temperature oscillations have comparable amplitudes ($D \approx \Theta$) and are almost exactly out of phase ($\alpha \approx \pi/2$).

[29] **Acknowledgments.** We thank H. J. Singer and two anonymous reviewers for insightful comments and helpful suggestions. This work has been supported in part by the NASA Heliophysics Theory and Living With a Star (LWS) programs as well as the Air Force Office of Scientific Research (AFOSR) Multidisciplinary University Research Initiative (MURI) program.

[30] Robert Lysak thanks John Meriwether and Federico Herrero for their assistance in evaluating this manuscript.

References

- Akmaev, R. A. (2001), Seasonal variations of the terdiurnal tide in the mesosphere and lower thermosphere: A model study, *Geophys. Res. Lett.*, *28*, 3817–3820.
- Akmaev, R. A., and H.-M. H. Juang (2008), Using enthalpy as a prognostic variable in atmospheric modelling with variable composition, *Q. J. R. Meteorol. Soc.*, *134*, 2193–2197.
- Akmaev, R. A., T. J. Fuller-Rowell, F. Wu, J. M. Forbes, X. Zhang, A. F. Anghel, M. D. Iredell, S. Moorthi, and H.-M. Juang (2008), Tidal variability in the lower thermosphere: Comparison of Whole Atmosphere Model (WAM) simulations with observations from TIMED, *Geophys. Res. Lett.*, *35*, L03810, doi:10.1029/2007GL032584.
- Akmaev, R. A., F. Wu, T. J. Fuller-Rowell, and H. Wang (2009), Midnight temperature maximum (MTM) in Whole Atmosphere Model (WAM) simulations, *Geophys. Res. Lett.*, *36*, L07108, doi:10.1029/2009GL037759.
- Arduini, C., G. Laneve, and F. A. Herrero (1997), Local time and altitude variation of equatorial thermosphere midnight density maximum (MDM): San Marco drag balance measurements, *Geophys. Res. Lett.*, *24*, 377–380.
- Behnke, R. A., and R. M. Harper (1973), Vector measurements of F region ion transport at Arecibo, *J. Geophys. Res.*, *78*, 8222–8234.
- Colerico, M. J., M. Mendillo, C. G. Fesen, and J. Meriwether (2006), Comparative investigations of equatorial electrodynamics and low-to-mid latitude coupling of the thermosphere-ionosphere system, *Ann. Geophys.*, *24*, 503–513.
- Deng, Y., A. J. Ridley, and W. Wang (2008), Effect of the altitudinal variation of the gravitational acceleration on the thermospheric simulation, *J. Geophys. Res.*, *113*, A09302, doi:10.1029/2008JA013081.
- Forbes, J. M., S. L. Bruinsma, Y. Miyoshi, and H. Fujiwara (2008), A solar terminator wave in the thermosphere neutral densities measured by the CHAMP satellite, *Geophys. Res. Lett.*, *35*, L14802, doi:10.1029/2008GL034075.
- Fuller-Rowell, T. J., et al. (2008), Impact of terrestrial weather on the upper atmosphere, *Geophys. Res. Lett.*, *35*, L09808, doi:10.1029/2007GL032911.
- Fuller-Rowell, T. J., F. Wu, R. A. Akmaev, T.-W. Fang, and E. A. Araujo-Pradere (2010), A Whole Atmosphere Model simulation of the impact of a sudden stratospheric warming on thermosphere dynamics and electro-dynamics, *J. Geophys. Res.*, doi:10.1029/2010JA015524, in press.
- Harper, R. M. (1973), Nighttime meridional neutral winds near 350 km at low to mid-latitudes, *J. Atmos. Terr. Phys.*, *35*, 2023–2034.
- Herrero, F. A., and N. W. Spencer (1982), On the horizontal distribution of the equatorial thermospheric midnight temperature maximum and its seasonal variation, *Geophys. Res. Lett.*, *9*, 1179–1182.
- Hines, C. O. (1960), Internal atmospheric gravity waves at ionospheric heights, *Can. J. Phys.*, *38*, 1441–1481.
- Liu, H., H. Lühr, V. Henize, and W. Köhler (2005), Global distribution of the thermospheric total mass density derived from CHAMP, *J. Geophys. Res.*, *110*, A04301, doi:10.1029/2004JA010741.
- Martinis, C., J. Baumgardner, S. M. Smith, M. Colerico, and M. Mendillo (2006), Imaging science at El Leoncito, Argentina, *Ann. Geophys.*, *24*, 1375–1385.
- Mayr, H. G., I. Harris, N. W. Spencer, A. E. Hedin, L. E. Wharton, H. S. Porter, J. C. G. Walker, and H. C. Carlson Jr. (1979), Tides and the midnight temperature anomaly in the thermosphere, *Geophys. Res. Lett.*, *6*, 447–450.
- Meriwether, J., M. Faivre, C. Fesen, P. Sherwood, and O. Veliz (2008), New results on equatorial thermospheric winds and the midnight temperature maximum, *Ann. Geophys.*, *26*, 447–466.
- Phillips, N. A. (1966), The equations of motion for a shallow rotating atmosphere and the “traditional approximation,” *J. Atmos. Sci.*, *23*, 626–628.
- Spencer, N. W., G. R. Carignan, H. G. Mayr, H. B. Niemann, R. F. Theis, and L. E. Wharton (1979), The midnight temperature maximum in the Earth’s equatorial thermosphere, *Geophys. Res. Lett.*, *6*, 444–446.
- Volland, H., and H. G. Mayr (1972), A three-dimensional model of thermosphere dynamics—I. Heat input and eigenfunctions, *J. Atmos. Terr. Phys.*, *34*, 1745–1768.
- Volland, H., and H. G. Mayr (1973), A numerical study of three-dimensional diurnal variations within the thermosphere, *Ann. Geophys.*, *29*, 61–75.

R. A. Akmaev, NOAA Space Weather Prediction Center, W/NP9, 325 Broadway, Boulder, CO 80305, USA. (rashid.akmaev@noaa.gov)

T. J. Fuller-Rowell, H. Wang, and F. Wu, CIRES, University of Colorado, 216 UCB, Boulder, CO 80309, USA.

M. D. Iredell, NOAA Environmental Modeling Center, 5200 Auth Rd., Camp Springs, MD 20746, USA.